Multichannel ATI-SAR with application to the adaptive Doppler filtering of ocean swell waves

B.C. Barber

Abstract: Multichannel along track interferometric (MATI) SAR systems are discussed from the point of view of ocean remote sensing. It is shown that the signals scattered by range moving scatterers can be Doppler filtered using a MATI-SAR. Processing techniques are presented, including a phase screen method for the removal of phase errors (including systematic errors and also those resulting from platform motions). A particular radar system (the ESR, enhanced surveillance radar) is described; this has a 3 cm wavelength MATI with two, three or four beams. It is used for investigating and exploiting Doppler effects in ocean radar scattering. It is demonstrated that, by applying adaptive Doppler filtering techniques, the MATI-SAR can significantly increase the imaging sensitivity of ocean features with respect to a conventional SAR. Examples illustrate the use of the ESR MATI-SAR system for imaging ship generated swell waves. Using three beams, the visibility of the wave images is increased by 9.5 dB looking downwind and 5.0 dB looking upwind for horizontal polarisation at grazing angles of 39° and 32°, respectively. Associated Doppler filter responses are shown which show that the scatterers modulated by the swell wave are located in the neighbourhood of the wave crests.

1 Introduction

Multi-aperture along track interferometric (MATI) SAR systems are a special case of the general class of multi-aperture coherent imaging radars. These radars can, in principle, reconstruct the three-dimensional range/azimuth/velocity image of any moving object [1, 2]. For the case of the ATI with two antennas it was shown in [3, 4] that the range component of surface ocean current velocity can be linearly related to the phase difference between the signals received by the two antennas provided the phase differences are small [5, 6], and provided a number of assumptions are made concerning the sea surface scattering mechanisms. Subsequently, the theory of multi-aperture systems has been developed and extended to the point where it can be demonstrated using analysis and simulation that such radars can measure ‘velocity maps’ of the sea surface [7] and Doppler spectra [8]. They can also measure the coherence time of the scatterers [9–11]. Another recent development is the use of two-frequency ATI to image the sea surface [12].

MATI systems can also be used to Doppler filter radar signals backscattered from the sea surface. Consider a MATI which has multiple pairs of antennas. Instead of just one phase difference measured by the two beam systems [3, 4] there is now a time sequence of phase differences from which a Doppler spectrum can be measured. Furthermore, images processed from the signals received by the antennas can be Doppler filtered by combining them in the same way as in the image plane of a multiaperture interferometer but with suitable phase and amplitude weighting to define the position and shape of the filter pass-band. This is useful because sea surface scatterers have associated Doppler spectra which depend on the type of scatterer [13]. For example, suppose that a certain class of scatterer is associated with energy located in a particular part of the Doppler spectrum, and that an image feature is the result of the modulation of this class of scatterer. Then it is possible, in principle, to adaptively change the position and shape of a Doppler filter pass-band to achieve optimum capture of the energy from the required scatterers and rejection of the remainder. Consequently, adaptive Doppler filtering via a MATI can be used to improve the visibility of features in SAR images of the sea surface and to gather useful information on the nature of the scattering mechanisms.

In this paper an experimental airborne MATI is described together with some of the processing techniques which have been developed to exploit the use of the system in imaging the ocean surface.

2 ESR interferometer system

The ideas discussed in the Introduction have been incorporated into a practical airborne radar system: the enhanced surveillance radar (ESR). Figure 1 shows a schematic diagram of this radar system imaging swell waves on the ocean surface.

The aircraft platform (a BAC/BAe 1-11) is equipped with a conventional synthetic aperture radar except that the radar echoes from the target are received by three or four antennas. Two extra antennas are placed about a metre in front and a metre behind the main radar antenna (these antenna spacings are fixed in flight but can be varied on the ground). In addition, the main antenna has a monopulse capability and can be split into two parts to provide two

IEE Proceedings online no. 20030935

doi: 10.1049/ip-rsn:20030935

Paper first received 19th September 2002 and in revised form 31st July 2003

The author is with the Defence Science and Technology Laboratory, MOD, A2 Building, Dstl Farnborough, Hants GU14 0LX, UK

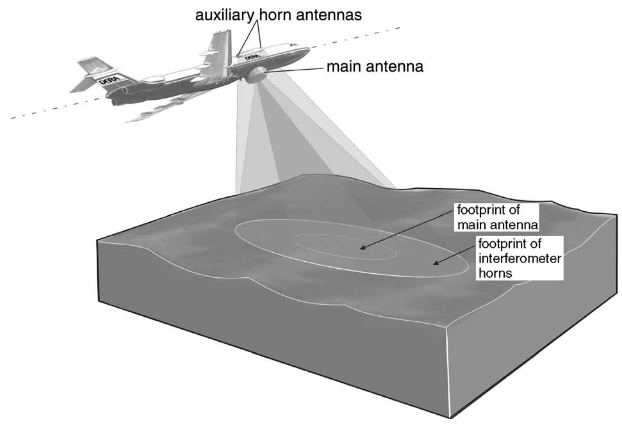

Fig. 1 *ESR system imaging swell waves*

further receive antennas. The results reported here were obtained using the sum signal from the main antenna and thus relate to three and two beams; some results using four beams are reported in [14]. The footprints of the three beams overlap and the main antenna is used to transmit and all three antennas are used to receive. The aircraft installation necessitated the use of small horns for the auxiliary antennas. This resulted in much larger footprints than the main antenna, as shown in Fig. 1. Some radar system parameters used in the work reported here are given in Table 1. More details of the ESR interferometer system are given in [14].

Synthetic aperture radar images are formed from the signals from each antenna. Exactly the same processing parameters (and processor) are used in the processing of each image; this ensures that any phase errors introduced by the processor and any phase functions which remain in the images are the same for each image. These images are analytic functions in complex form and there is a systematic phase shift between them due to the physical separation between the receiving antennas both along the aircraft track and across track. The across track variation comes about because the main and auxiliary antennas are located at different vertical locations on the airframe (see Fig. 1). The along track variation comes from aircraft yaw, pitch and roll motions. These range variations are functions of position and time and their effects are removed from the data using a phase screen technique. The images from the three antennas are initially formed into two two-beam interferometer images using pairs of images from fore and main and main and aft antennas. Thus the signals from the main antenna are always used as the phase reference. The interferometer images from each pair are formed in exactly the same way as in a two-beam optical interferometer [15]. So, if the complex-valued image at pixel location (p, q) resulting from the signals received by the front antenna is $F(p, q)$ and the image at the same location received by the main antenna is $M(p, q)$, then the interferometer image $G(p, q)$ is formed where

$$G(p, q) = |F(p, q) + M(p, q)|^2 \qquad (1)$$

Figure 2 shows an image of the sea surface which results from the fore and main antenna pair. The interference fringes represent a two-dimensional phase function or 'phase screen' $\phi(p, q)$; they can be removed from $G(p, q)$ by multiplying $F(p, q)$ by the conjugate phase screen function $\exp[-i\phi(p, q)]$. The three images from the antennas are phase compensated and combined to form an image $H(p, q)$, where

$$H(p, q) = |F(p, q)\exp[-i\phi(p, q)] + M(p, q) + A(p, q)\exp[-i\psi(p, q)]|^2 \qquad (2)$$

and $\exp[-i\psi(p, q)]$ is the conjugate phase screen for the main and aft image pair. This phase screen technique sets the mean phase difference for each image pair to zero and in consequence the Doppler spectra are shifted to zero baseband.

Suppose that the three antennas receive perfectly coherent plane electromagnetic waves of unit amplitude scattered by a moving object. If the Doppler frequency due to the motion of the scatterers is ν and the time interval between the antennas is Δt (which equals the antenna along track separation divided by the aircraft speed), then the phase shift θ caused by scatterer motion is $\theta = \pi\nu\Delta t$. The reason that there is no factor of two in the expression for θ is that, due to the 'monostatic–bistatic equivalence theorem' [16], Δt has to be halved because, for small angles, the radar views the scattering object as if it were located midway between the antennas. On substituting into (2), and assuming that phase errors have been compensated, the power spectral response of a band-pass filter with centre frequency ν_0 to the Doppler frequencies ν of the scatterers is

Table 1: ESR Radar system parameters

Wavelength	3.0 cm
Polarisation	HH
Azimuth resolution	1.0 m
Slant range resolution	1.2 m
Main antenna one way beamwidth	
in azimuth	1.32°
in range	7.0°
Auxiliary antenna one way beamwidth	
in azimuth	28.0°
in range	28.0°
Main antenna stabilisation error	0.1° rms max.
Pulse width	5 μs
Peak power	15 kW
Effective PRF for each receive channel	500 Hz
Typical aircraft speed	125 m/s

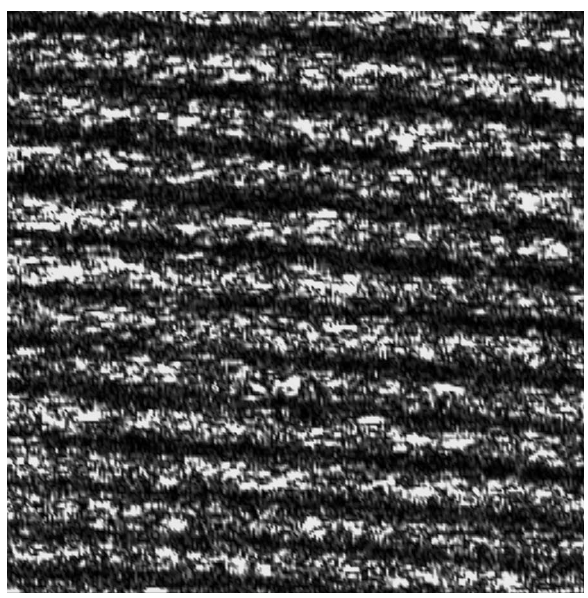

Fig. 2 *Interference fringes from fore and main antennas*

$$I(\nu) = |\exp[-i\pi(\nu-\nu_0)\Delta t] + 1 + \exp[+i\pi(\nu-\nu_0)\Delta t]|^2$$
$$= |\sin[3\pi(\nu-\nu_0)\Delta t/2]/\sin[\pi(\nu-\nu_0)\Delta t/2]|^2 \quad (3)$$

In actual practice a more general view of the filter is adopted and both the phase and amplitude of the filter coefficients are changed adaptively to enhance the images of certain sea surface scatterers (explained below). Such processing has previously been employed for interference suppression and clutter cancellation [17, 18]. Here, however, the adaptive processing is used to enhance one part of the clutter spectrum relative to the rest of the clutter spectrum.

3 Phase correction technique

Figure 3 shows a block diagram of the overall interferometric filter processing scheme. First, the images are displaced relative to each other along track and in range as a result of using identically the same range history in the processing. The auxiliary images therefore have to be collocated with the main antenna image using an interpolation and resampling process, and this is shown in the block at the top of Fig. 3. Next, the auxiliary images have to be phase corrected relative to the main antenna image as explained in Section 2, and this is shown in the next block down in Fig. 3. The third block in Fig. 3 shows the adaptive filtering and this process is summarised by the diagram in Fig. 4.

3.1 Construction of first phase screen

The interferometer fringes are a consequence of phase variations only. Hence the first step in constructing a conjugate phase screen is to set the modulus of each pixel to unity to remove envelope modulations, but preserving the phase.

The fringes are essentially modulated intensity speckle patterns, as are the image scatterer modulations. When using fringe patterns such as those in Fig. 2 to define a phase screen the scatterer phase modulations have to be smoothed to leave only the fringes. Clearly, in smoothing the scatterer phase modulations the interference fringes should be as broad as possible so that the scale lengths of scatterer modulations and the scale lengths of the fringes are as widely separated as possible. The differential phase shifts leading to the fringes are a result of the physical antenna separation, the imaging geometry and the linear and rotational velocities of the aircraft. The differential phase shifts resulting from the antenna separation and imaging geometry are easily predictable and aircraft motion can be measured using an inertial platform. An approximate initial phase screen can therefore be constructed which can be used to remove the majority of the phase shifts. The result of applying the initial screen is that the residual phase differences are more slowly varying. The residual fringes are thus broader, and speckle smoothing can be done using a wider smoothing kernel and so is more effective. This is discussed further in Section 3.2. The same initial phase screen is used for all the auxiliary images as a matter of convenience; any residual errors are taken out by the second phase screen.

The two auxiliary antennas were arranged symmetrically either side of the main antenna, and the aircraft installation required that the auxiliary antennas were situated above the main antenna. Consider a vertical plane containing the main antenna focus, the plane being orthogonal to the longitudinal axis through the airframe. Define l as the distance between the focus of the main antenna and the foci of the auxiliary antennas projected on to the plane and measured in the plane. Define χ as the angle between the line connecting the main antenna focus and auxiliary antenna foci in the plane and the vertical, and let the incidence angle of the radar beam centre at the target at the minimum range be ξ. An approximate formula for the change in phase with slant range across the interferometer image is then, to first order,

$$P(r) = \exp i2\pi\left[\frac{l}{\lambda}\frac{\sin(\xi+\chi)}{\tan\xi}\frac{r_o}{r} + \frac{l}{\lambda}\Delta\zeta\sin(\xi+\chi) + \frac{s}{\lambda}\Delta\eta\sin\xi\right] \quad (4)$$

where r_o is the range at the near edge of the image (or any suitable reference point), r is the range across the image and λ is the radar wavelength. Also, $\Delta\zeta$ and $\Delta\eta$ are small changes in the roll and yaw angles and $2s$ is the separation between the foci of the auxiliary antennas projected orthogonally on to a horizontal plane containing the main antenna focus. Pitch angle changes only have a second order effect on the phase shifts and have been neglected in (4). Note that any residual errors are removed by the second screen and so the estimates of aircraft motion do not need to be of high precision. Equation (4) defines the first order phase screen and the image is multiplied by the complex conjugate of (4) to produce a set of broadened fringes. Transverse velocity components have been neglected in (4); the reasons for this are explained below in connection with the second phase screen.

The process described above is illustrated by the images in the top line of Fig. 5. This Figure relates to the first example in Section 4. In each image in Fig. 5 the x co-ordinate is the along track direction and the y co-ordinate is the range. Figure 5*a* shows the fringes obtained from the fore and main antennas in this instance. Figure 5*b* shows the (unwrapped) initial screen defined by (4) and Fig. 5*c* shows the resultant fringes after applying the initial phase screen. It will be seen from the residual phase shown Fig. 5*c* that the initial phase screen is quite successful in removing most of the phase fluctuations. Images in Figs. 5*a–c* are each

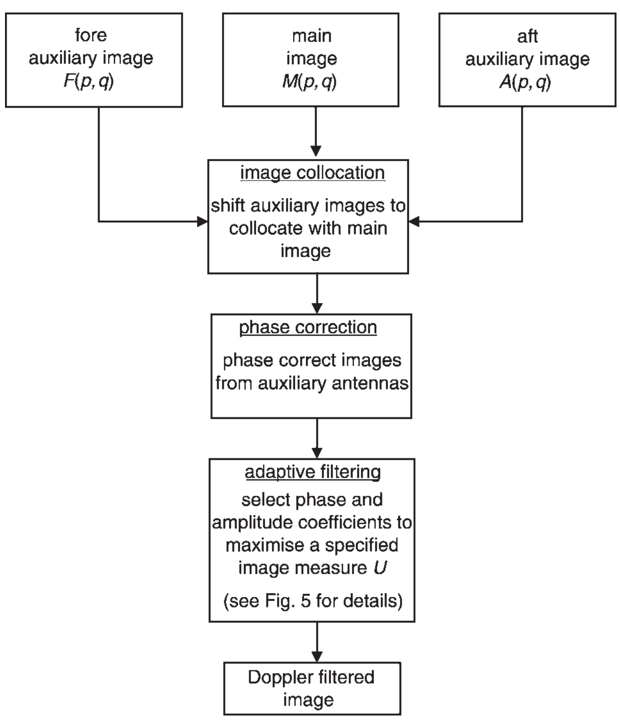

Fig. 3 *Block diagram of overall processing scheme*

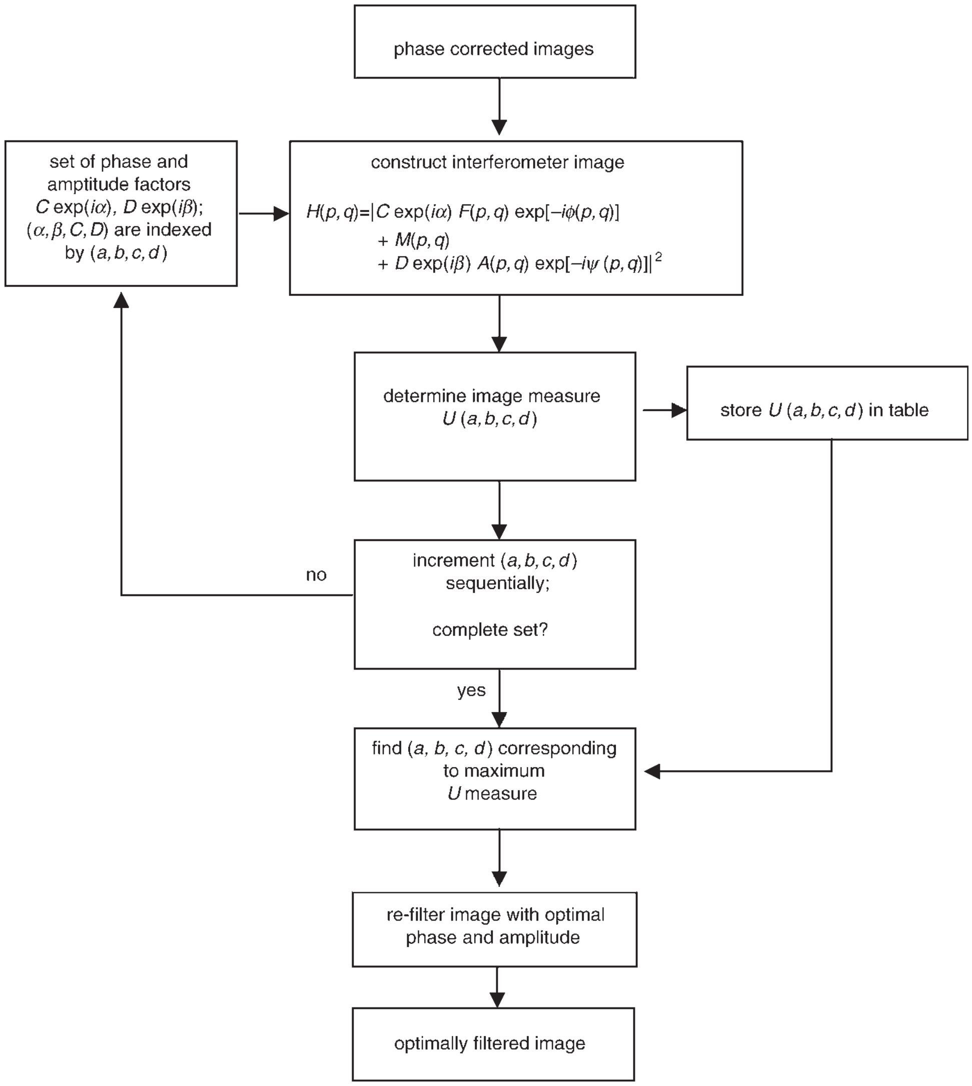

Fig. 4 *Diagram showing adaptive filtering process*

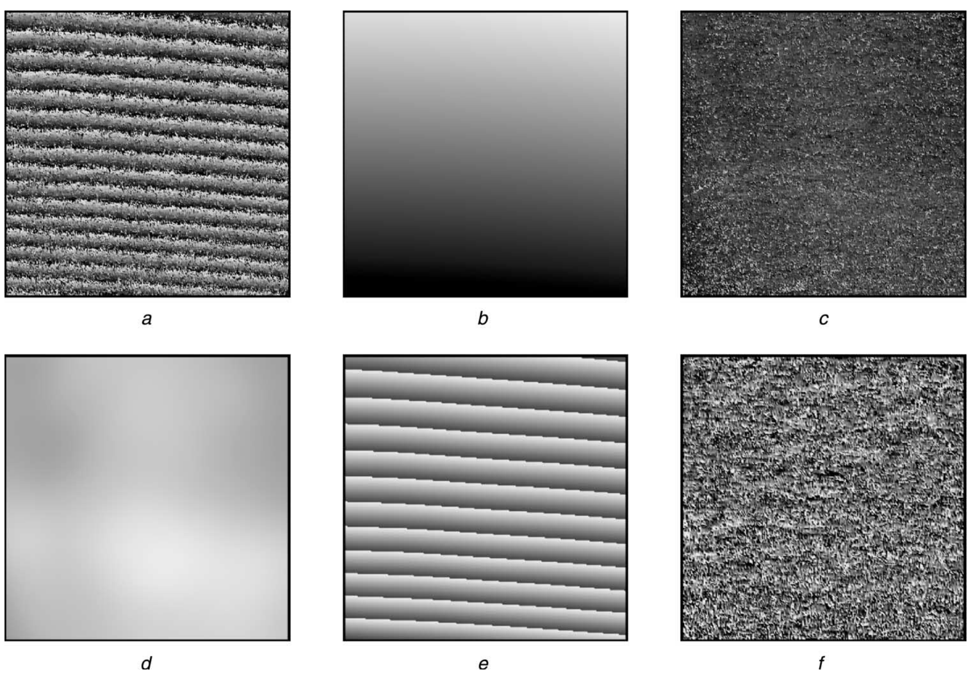

Fig. 5 *Phase screen generation*

356 pixels square (427.2 m in slant range and ~356 m along track).

3.2 Second phase screen

The speckled fringes resulting from the first phase screen have to be smoothed and this is achieved by convolving the real and imaginary points of the image separately with a smoothing function. The function used here was a raised cosine. The size of the kernel to the zero points was 50 pixels in each direction in this case. The phase defined by the argument of the smoothed real and imaginary points gives the second phase screen. This is shown in Fig. 5*d*. Note that, although this image appears to be the same size as the previous images, it is in fact smaller by twice the width of the smoothing kernel (i.e. 256 pixels square) because the partially smoothed edges have been deleted. This is also true of the remaining images. The residual phase function is then combined with the initial phase screen (which is clipped to make it the same size) to produce the final screen shown in the bottom centre of Fig. 5*e*. The raw interferometer image is then operated on by the complex conjugate of the final screen to produce the final corrected image, the residual phase of which is shown Fig. 5*f*. Patterns corresponding to image feature phase modulations tend to be visible in the residual phase only for strong features. There are traces of swell wave modulations visible in Fig. 5*f*, and these correspond to the first of the examples presented in Section 4 (as does the whole of Fig. 5). Usually the modulations are swamped by phase fluctuations from unmodulated scatterers (and it is the aim of the filtering process to attenuate the Doppler spectrum corresponding to these unmodulated scatterers).

The scale size of the smoothing kernel is important. The smoothing process leaves a local mean phase which follows the fringes and so the scale size needs to be small in comparison with the width of the fringes. On the other hand, the kernel size needs to be large in comparison with the local phase fluctuations caused by the scatterers in order to achieve effective smoothing. This means that large scale phase variations such as those produced by large scale currents on which the two beam velocimetry technique depends [3, 4] will be removed by the conjugate second phase screen. On the other hand, individual scatterers which are modulated by larger scales, say a sandbank or a swell wave, and which have 'local' amplitude and phase variations with a scale length much less than the kernel will not be affected by the conjugate phase screen. Hence, image amplitude modulations will be retained even if they have a scale length greater than the kernel.

The phase offsets caused by constant aircraft transverse velocity components will be removed by the conjugate second screen in the same way as constant ocean background currents. In addition, when the aircraft is buffeted by gusts and turbulence the resulting phase fluctuations are also removed. The aircraft can be considered to be a low-pass filter with an input represented by gust and turbulence forces and an output represented here by the phase fluctuations. The decorrelation time of the phase fluctuations depends on the size (and inertia) of the aircraft and is typically 5-10 s for the BAC1-11. The aircraft travels a distance of the order of 1 km in this time and the decorrelation length of the phase fluctuations is thus much greater than the smoothing kernel size so such phase fluctuations are removed. However, if the amplitude of the turbulence is great enough there will be a degradation in interferometer filter performance.

4 Filtering technique and results

Following the removal of the phase errors, the residual phase differences contained in the images represent the Doppler information which is exploited by the interferometer technique in band-pass filtering the Doppler spectrum. Equation (2) gives the image function $H(p, q)$ for uniformly weighted images from the three antennas. In general, if the fore and aft antennas are weighted by $C\exp(i\alpha)$ and $D\exp(i\beta)$, respectively, then the image function is

$$H(p,q) = |C\exp(i\alpha)F(p,q)\exp[-i\phi(p,q)] + M(p,q) + D\exp(i\beta)A(p,q)\exp[-i\psi(p,q)]|^2 \tag{5}$$

The basic idea is then to combine the images, and systematically change the complex weighting factors until a given image measure contained in $H(p, q)$ is maximised (or minimised). The phase screen technique sets the mean phase difference between antenna pairs to zero and so the mean Doppler frequency in a given image is also zero: the Doppler spectrum is essentially shifted to zero baseband. This must always be borne in mind when interpreting the Doppler spectra.

The filtering process is shown in block diagram form in Fig. 4. It is implicit in Fig. 4 that there is a finite set of parameters (α, β, C, D) with integer indices (a, b, c, d). Experience of using this technique for sea surface images has shown that keeping the amplitudes (C, D) constant and varying only the phases (α, β) leads to a loss of from 0 to 0.5 dB in the maximised image measure.

4.1 Examples of swell wave filtering

Figure 6 shows a slant range image, 256 pixels square, of a small area of sea about 25 km east of Ramsgate in the southern North Sea. The radar grazing angle was about 32.3° at the image centre, the range to the image centre was 1983 m and the aircraft speed was 128 m/s. The image is an amplitude (modulus) SAR image from the main antenna of the ESR. Field observations taken at the time of the image showed that the wind was blowing towards the radar at an angle of 30° to the across track direction with a speed of 7 m/s at 10 m height. The image shows the surface gravity waves generated by a ship travelling down-range. The ship is located about 1 km down-range of the image centre, measured on the surface. The image location has been chosen so that the waves are travelling almost exactly away

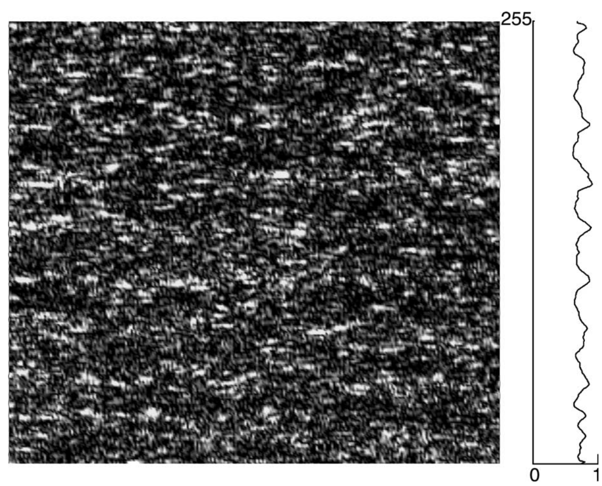

Fig. 6 *Image of ship generated swell waves moving away from radar*

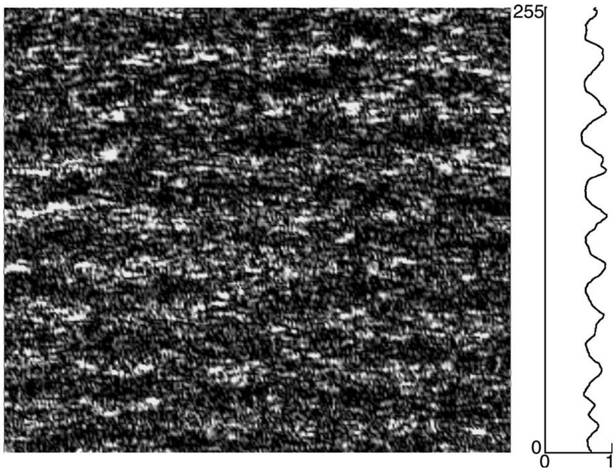

Fig. 7 *Three-beam filtered version of Fig. 6*

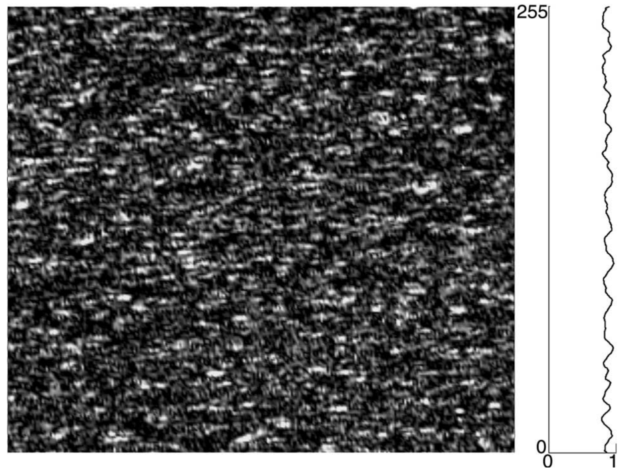

Fig. 9 *Image of ship generated swell waves moving towards the radar*

from the radar. The vertical scale on the right of the image shows the row averages and hence the average wave amplitude modulation. There are about 8.7 waves in the image and the range sample size is 1.2 m, so the wavelength on the sea surface is 41.8 m. Such a wave has a phase speed of 8.08 m/s in deep water. Figure 7 shows the same image with filtering applied using three beams and varying only the phases of the weights (the moduli of the weights being kept constant and equal). The average improvement in wave modulation is ~5.0 dB as evidenced by the row average scale on the right hand side. The filter weights which maximised the wave modulation have been used to compute the equivalent power spectral response shown by the solid line in Fig. 8. The peak is located at −57 Hz. Also shown in Fig. 8 are the filter responses which result from the two-beam interferometers using the fore/aft pair (long dashed line) and the fore/main or main/aft pairs (short dashed line). These two last pairs gave slightly different phases so the filter response was computed on the basis of their average phase shift. The performance of the two-beam filters was almost as good as the three-beam filter, the fore/aft pair giving 4.5 dB and the fore/main and main/aft pairs giving an average of 3.7 dB. Note that the separation of the fore and aft antennas was 2 m and that of the fore/main and main/fore antennas was 1 m. Hence the (sinusiodal) response curve for the fore/aft pair has two cycles over the spectrum and the other response curves have one cycle.

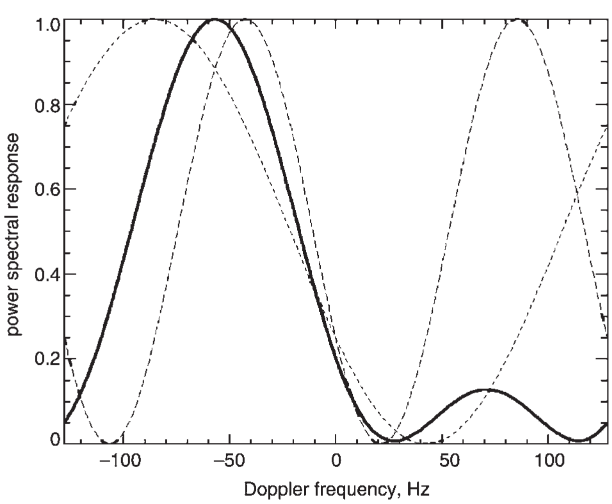

Fig. 8 *Power spectral response corresponding to Fig. 7 (solid line)*

Figure 9 shows a patch of sea shifted in the direction of the ship by about 400 m relative to Fig. 6 (but in the same along track location to within ~100 m). The aircraft has flown around through 180° and the waves are now travelling towards the radar. It was not possible to select waves travelling exactly in the range direction in this case. Consequently the waves in Fig. 9 are travelling at an angle of 5.7° to the across track direction, and Figs. 9 and 10 have been rotated by this angle. The image size is again 256 pixels. The grazing angle at the image centre was 39.2°, the range to the image centre was 1601 m and the aircraft speed was 123 m/s. This image is about 411 s after Fig. 6 and the ship was located nearly 4 km up-range (measured on the surface) of the centre of Fig. 9. This distance is approximately four times the 1 km ship to image centre distance in Fig. 6. Hence these waves are much smaller in amplitude than those in Fig. 6 (theoretically by a factor of two on the basis of wave energy conservation because (i) they are ship generated and the wake area expands linearly with time and (ii) the wave energy per unit crest length is proportional to wave amplitude squared). This is one reason why they are almost invisible: in fact, if one did not know that the waves existed there would be no reason to suppose that they did on the evidence of Fig. 9. Figure 10 shows the three-beam filtered (again phase only) version of Fig. 9 and the waves are now visible. In fact the waves imaged in Fig. 10 have about half the amplitude of the waves imaged in Fig. 7, in agreement with the above wave

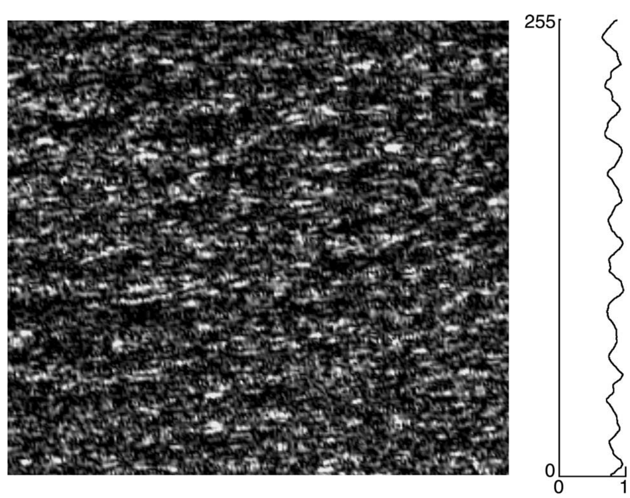

Fig. 10 *Three-beam filtered version of Fig. 9*

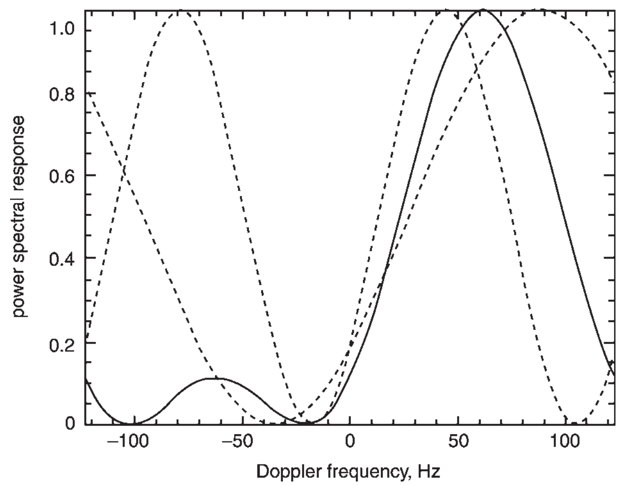

Fig. 11 *Power spectral response corresponding to Fig. 10 (solid line)*

attenuation argument. The improvement in image modulation is ~9.5 dB (measured from Fourier transforms in this case). There are 10.0 waves in the image and this corresponds to a wavelength on the sea surface of 39.6 m, which is 5% lower than the previous estimate. This is well within possible cumulative experimental and approximation errors (which could easily exceed 10%). The filter response resulting from the phase weights is shown by the solid curve in Fig. 11 and the peak of the response is now located at +61 Hz. The filter response which results from using only the fore/aft pair is again shown by the long dashed line and the fore/main or main/aft pairs by the short dashed line. The fore/aft pair gave an improvement of 9.2 dB and the fore/main and main/aft pairs gave 7.3 dB.

4.2 Discussion

For a linear sinusoidal wave a point on the surface describes a circle with a fixed centre as the wave moves beneath it. The diameter of the circle equals the peak-to-trough amplitude of the wave and the angular frequency of the circular motion equals that of the wave. At the crest of the wave the velocity vector points in the direction of wave propagation. Suppose that a line is drawn from the radar antenna focal point through the centre of the circle. It is immediately apparent that those scatterers lying on the circle located above the line have positive Doppler shifts and those below the line have negative Doppler shifts when the wave is travelling towards the radar (and *vice versa*). It was pointed out above that the phase screen technique shifts the measured Doppler spectrum to zero baseband. Hence the Doppler spectra in Figs. 8 and 11 indicate frequencies relative to the mean frequency of the total spectrum, and this is generally not zero [13]. However, if a linear superposition of frequencies is assumed, then the swell waves produce Doppler frequencies superposed on the mean background frequency. It then becomes clear that those scatterers which are modulated by the swell waves and detected by the radar are located above the line in each case and may thus be loosely associated with the wave crests. Also, notice that the second peak in the two-beam (fore/aft) filter appears to have little impact on the filter performance, the loss over three beams being 0.5 dB and 0.3 dB for the above examples. This implies that there is negligible scatterered energy in the neighbourhood of this spectral peak (which corresponds to scattering from below the line in the neighbourhood of the wave troughs).

In principle it is possible to measure the amplitude of the waves given their wavelength and the peak Doppler shifts. As pointed out above the relative wave amplitudes in Figs. 7 and 10 agree with a simple wave attenuation argument. This indicates a linear imaging mechanism and gives encouragement to continue with this argument. However, the filter responses shown in Figs. 8 and 11 probably have as much to do with stopping the Doppler band associated with 'bad' (i.e. unmodulated) scatterers as passing the band associated with 'good' scatterers. This becomes clear when the two-beam and three-beam responses are compared. The 'stop-bands' of the three- and two (fore/aft)-beam filters almost coincide in both Figs. 8 and 11. Furthermore, the factor of two difference in amplitude in Figs. 7 and 10 would lead to a corresponding difference in peak Doppler shift relative to the mean background Doppler frequency, all else being equal. This Doppler shift is not borne out by the computed filter responses. This question can only be resolved conclusively by using a higher order filter with more antenna beams, giving a sharper response.

It should be added that, although the three- and two (using the fore/aft antennas)-beam filters gave almost the same performance in this instance, this is not in general true in all situations for all types of ocean image. Furthermore, the use of four beams sometimes gives a greater increment in performance over three beams than three does over two. Signals from the main antenna difference channel were not recorded in the above examples and so four-beam data is not available for comparison in this instance. This issue will be addressed further in future studies.

5 Conclusions

Phase compensation and error removal techniques have been developed for multiaperture along track interferometer image sets. Synthetic aperture images processed from the receiving antennas are taken in pairs (fore–main and aft–main in the case of three antennas), one of the images always being taken as the phase reference. Initial phase screens are set up for each pair to remove most of the systematic phase differences resulting from across track antenna separation and aircraft attitude angle changes. The remaining phase differences are smoothed and a second phase screen constructed for each antenna pair. This final screen then removes the remaining phase errors. The technique shifts the Doppler spectrum so that the mean Doppler frequency is zero. Hence constant background Doppler shifts due to large scale ocean currents and constant aircraft transverse velocity components are removed. This double phase screen technique is shown to work well and does not require high precision measurements of the aircraft motion.

Combining the phase compensated images interferometrically then results in the images being Doppler band-pass filtered. The shape and centre frequency of this filter can be varied by varying the amplitude and phase weighting of the corrected images. An adaptive processing technique is described in which the phase and amplitude weighting of the phase compensated images is varied until the visibility of a selected image feature is maximised. Examples are presented of the maximisation of the visibility of ship generated swell waves. The swell wave visibility is taken to be the ratio of the peak of the power spectrum of the modulus (i.e. amplitude) image at the relevant swell wavevector to the mean spectral power less the zero frequency component. It is demonstrated that using three beams for the presented examples, the swell wave visibility is improved by a factor of 5.0 dB looking upwind and 9.5 dB looking downwind at grazing angles of 32.3° and 39.2° using horizontal polarisation. Doppler filter response functions for these examples show that the scatterers with increased scatter cross-section which are modulated by the swell wave are located in the neighbourhood of the wave crests. For the presented examples the use of two beams (the fore and aft auxiliary antennas) results in a loss of only 0.3 dB to 0.5 dB.

6 Acknowledgment

This work was funded by the Ministry of Defence. The author thanks Bob Hill at QinetiQ Malvern for processing the ESR images, Shane Rouse at QinetiQ Malvern for data on the ESR system, and Jonathan Perry and Giles Gibson at Dstl Farnborough for environmental measurements. Thanks are also due to Keith Ward of TWR at Malvern for bringing the author's attention to Reference 16, and for many useful discussions.

7 References

1 Friedlander, B., and Porat, B.: 'VSAR: a high resolution radar system for detection of moving targets', *IEE Proc., Radar Sonar Navig.*, 1997, **144**, (4), pp. 205–218
2 Orwig, L.P., and Held, D.N.: 'Interferometric ocean surface mapping and moving object relocation with a Norden Systems Ku-band SAR'. Proc. IEEE Int. Geoscience and Remote Sensing Symp., 1992
3 Goldstein, R.M., and Zebker, H.A.: 'Interferometric radar measurements of ocean surface currents', *Nature*, 1987, **328**, pp. 707–709
4 Goldstein, R.M., Barnett, T.P., and Zebker, H.A.: 'Remote sensing of ocean currents', *Science*, 1989, **246**, pp. 1282–1285
5 Thompson, D.R., and Jensen, J.R.: 'Synthetic aperture radar interferometry applied to ship generated internal waves in the 1989 Loch Linnhe experiment', *J. Geophys. Res.*, 1993, **98**, (C6), pp. 10259–10269
6 Barber, B.C.: 'The phase statistics of a multichannel radar interferometer', *Waves Random Media*, 1993, **3**, pp. 257–266
7 Friedlander, B., and Porat, B.: 'VSAR: a high resolution radar system for ocean imaging', *IEEE Trans. Aerosp. Electron. Syst.*, 1998, **34**, (3), pp. 755–776
8 Lombardini, F., Gini, F., and Matteucci, P.: 'Multibaseline ATI-SAR for robust ocean surface velocity estimation in presence of bimodal Doppler spectrum'. Proc. IEEE Int. Geoscience and remote sensing Symp., 2001
9 Griffin, M.F., Bornan, E.C., Metal, I., and Orwig, L.P.: 'Estimating ocean-scene coherence time with a multi-aperture SAR'. Proc. IEEE Int. Conf. on Acoustics, speech and signal processing, 1993, pp. 461–464
10 Besson, O., Gini, F., Griffiths, H.D., and Lombardini, F.: 'Estimating ocean surface velocity and coherence time using multichannel ATI-SAR systems', *IEE Proc., Radar Sonar Navig.*, 2000, **147**, (6), pp. 299–308
11 Carande, R.E.: 'Estimating ocean coherence time using dual-baseline interferometric synthetic aperture radar', *IEEE Trans. Geosci. Remote Sens.*, 1994, **32**, (4), pp. 846–854
12 Kim, D., Moon, W.M., Imel, D.A., and Moller, D.: 'Remote sensing of ocean waves and currents using NASA (JPL) AIRSAR along-track interferometry (ATI)'. Proc. AIRSAR Earth Science and Application Workshop, Pasadena, CA, USA, 2002
13 Lee, P.H.Y., Barter, J.D., Beach, K.L., Hindman, C.L., Lake, B.M., Rungaldier, H., Shelton, J.C., Williams, A.B., Yee, R., and Yuen, H.C.: 'X band microwave backscattering from ocean waves', *J. Geophys. Res.*, 1995, **100**, (C2), pp. 2591–2611
14 Barber, B.C.: 'Ocean imaging using multichannel along track interferometry'. Proc. RADAR, Adelaide, Australia, 2003
15 Born, M., and Wolf, E.: 'Principles of optics' (CUP, UK, 1999, 7th edn.)
16 Kell, R.E.: 'On the derivation of bistatic RCS from monostatic measurements', *Proc. IEEE*, 1965, **53**, pp. 983–988
17 Klemm, R.: 'Space-time adaptive processing' (IEE, UK, 1998)
18 Ender, J.H.G.: 'Space-time adaptive processing for synthetic aperture radar'. Digest of IEE Colloq. Space–time adaptive processing, London, April 1998, pp. 6/1–6/18